THE JOURNAL OF PHYSICAL CHEMISTRY C
Article
Cite This: J. Phys. Chem. C 2018, 122, 20888−20893
pubs.acs.org/JPCC

In Situ Control of the Adsorption Species in CO_2 Hydrogenation: Determination of Intermediates and Byproducts

Kun Zhao,*[,†,‡] Ligang Wang,[§] Marco Calizzi,[†,‡] Emanuele Moioli,[†,‡] and Andreas Züttel*[,†,‡]

[†]Laboratory of Materials for Renewable Energy, Institute of Chemical Sciences and Engineering, Basic Science Faculty (SB), École Polytechnique Fédérale de Lausanne (EPFL), 1951 Sion, Switzerland

[‡]Swiss Federal Laboratories for Materials Science and Technology (EMPA), 8600 Dübendorf, Switzerland

[§]Group of Energy Materials (GEM), Institute of Mechanical Engineering (IGM), School of Engineering (STI), École Polytechnique Fédérale de Lausanne (EPFL), 1951 Sion, Switzerland

Supporting Information

ABSTRACT: CO_2 hydrogenation over catalysts is a potentially exciting method to produce fuels while closing the CO_2 cycle and mitigating global warming. The mechanism of this process has been controversial due to the difficulty in clearly identifying the species present and distinguishing which are reaction intermediates and which are byproducts. We in situ manipulated the independent formation and hydrogenation of each adsorption species produced in CO_2 hydrogenation reaction over Ru/Al_2O_3 using operando diffuse reflectance infrared Fourier transformation spectroscopy (DRIFTS) and executed a novel iterative Gaussian fitting procedure. The adsorption species and their role in the CO_2 hydrogenation reaction have been clearly identified. The adsorbed carbon monoxide (CO*) of four reactive structures was the key intermediate of methane (CH_4) production. Bicarbonate (HCO_3^-*), formed on the metal−support interface, appeared to be not only the primary product of CO_2 chemisorption but also a reservoir of CO* and consisted of the dominate reaction steps of CO_2 methanation from the interface to the metal surface. Bidentate formate (Bi-$HCOO^-$*) formed on Ru under a certain condition, consecutively converting to CO* to merge into the subsequent methanation process. Nonreactive byproducts of the reaction were also identified. The evolution of the surface species revealed the essential steps of the CO_2 activation and hydrogenation reactions which were inevitably initiated from HCO_3^-* to CO* and finally from CO* to CH_4.

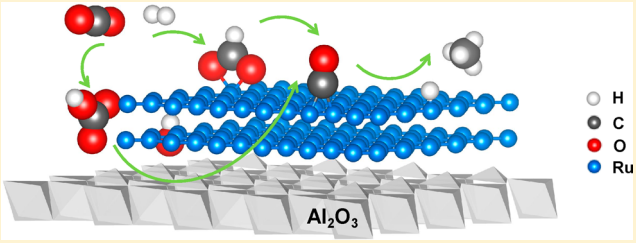

1. INTRODUCTION

CO_2 reduction by H_2 is a promising way to store hydrogen energy in hydrocarbons, producing synthetic fuels that exhibit the same energy density as fossil fuels to meet the increasing energy demands.[1,2] Moreover, the use of CO_2 as feedstock allows closure of the CO_2 cycle, reducing CO_2 emission and alleviating global warming. The mechanisms of CO_2 hydrogenation have been widely investigated on supported group VIII metals such as Ni, Ru, and Rh.[3−8] One of the principal analytical methods used is infrared spectroscopy, particularly diffuse reflectance infrared Fourier transformation spectroscopy (DRIFTS) for studying both the gaseous phase and the adsorption species on the catalyst surface. The main product is commonly found to be gaseous CH_4. However, various reaction mechanisms have been proposed, referring to different intermediates. Gaseous CO and adsorbed CO* were considered as important intermediates of CO_2 methanation because the well-known reversed water gas shift (RWGS) reaction could take place in the path of CH_4 production.[9−12] Some research has found that gaseous CO is not an intermediate as CO_2 was produced without visible occurrence of gaseous CO.[13,14] Instead, the adsorbed CO*, which is formed via surface RWGS reaction, is more favorable to be the intermediate as the adsorbed CO* exhibits relation with CH_4 formation.[15−19] However, other research also supports that the adsorbed formate ($HCOO^-$*) is the intermediate rather than CO*.[20] The mechanism of CO_2 hydrogenation is still controversial.

There are two key problems with the previous work: difficulties in the definitive determination of the species that appear during the reaction and difficulty with knowing whether a given species is an intermediate or a byproduct of CO_2 methanation.

To address the first problem, we resolved the peaks of the adsorbates using Gaussian fittings which were iteratively improved to produce a consistent view of the trends in observed species. To address the second problem, we controlled the formation of each adsorption species in situ, followed by reducing the obtained adsorption species individually in H_2 to monitor their role in the hydrogenation process. This allowed us to trace the origin and reaction path of each adsorption species and to determine the key

Received: July 7, 2018
Revised: July 26, 2018
Published: August 8, 2018

DOI: 10.1021/acs.jpcc.8b06508
J. Phys. Chem. C 2018, 122, 20888−20893

intermediate of CO_2 methanation. We found that the essential pathway of CO_2 activation was $CO_2 \rightarrow HCO_3^{-}* \rightarrow CO*$ whether H_2 was present or not. The surface RWGS reaction and $HCOO^{-}*$ contributed to CO* formation only when the system had abundant CO_2 and H_2. CO* was the key intermediate of CO_2 methanation. Besides, the reactivities of the adsorption species were adsorption-structure-dependent.

2. EXPERIMENTAL SECTION

Chemicals and Apparatus. The experiments were performed on ground Ru/Al_2O_3 (Sigma-Aldrich, 0.5 wt % loading on 3.2 mm pellets) or Al_2O_3 (Sigma-Aldrich). The infrared spectra were recorded using a Bruker Tensor 27 spectrophotometer with a resolution of 2 cm^{-1}, equipped with the Praying Mantis accessory and high-temperature reaction chamber (HVC) from Harrick Scientific for the diffuse reflectance infrared Fourier transformation spectroscopy (DRIFTS). The chamber was connected to He (purity 99.999%), H_2 (purity 99.999%), and CO_2 (purity 99.998%) gas lines and a turbomolecular pump. The tubing and the chamber were heated at 100 °C under vacuum overnight after loading the sample. The background pressure was 1×10^{-5} mbar. The spectrophotometer was continuously flushed with clean dry compressed air.

Sample Preparation. Ru/Al_2O_3 and Al_2O_3 was prereduced in the DRIFTS cell in H_2 flow with heating from room temperature (RT) to 350 °C at a heating rate of 2 °C/min and maintained at 350 °C for 4 h to remove the surface oxides on the Ru metal. The sample was then allowed to cool to RT in H_2 flow. A high vacuum of 1×10^{-5} mbar was recovered after pumping.

Experiments Performed. Following the pretreatment, seven sets of experiments were done: **Exp. I** CO_2 hydrogenation reaction. This was initiated by mixing 200 mbar of CO_2 and 800 mbar of H_2 at RT and heated to 300 °C with a rate of 1 °C/min on both Ru/Al_2O_3 and Al_2O_3. **Exp. II** CO_2 adsorption reaction. This was initiated by mixing 200 mbar of CO_2 and 800 mbar of He at RT, followed by heating to 300 °C with a rate of 1 °C/min on both Ru/Al_2O_3 and Al_2O_3. **Exp. III** $HCO_3^{-}*$ decomposition reaction. This was initiated by mixing 200 mbar of CO_2 and 800 mbar of He at RT, followed by pumping to high vacuum of 5×10^{-5} mbar, then heating to 300 °C with a rate of 1 °C/min on Ru/Al_2O_3. **Exp. IV** CO* hydrogenation. This was obtained directly from a $HCO_3^{-}*$ decomposition experiment at 300 °C, followed by cooling to RT, then filling with 1 bar of H_2 and heating to 300 °C with a rate of 1 °C/min on Ru/Al_2O_3. **Exp. V** $HCO_3^{-}*$ hydrogenation reaction. This was initiated by mixing 200 mbar of CO_2 and 800 mbar of He at RT, followed by pumping to high vacuum of 5×10^{-5} mbar, then filling the cell with 1 bar of H_2 and heating to 300 °C with a rate of 1 °C/min on Ru/Al_2O_3. There are also two experiments which were done without reducing the surface: **Exp. VI** HCOOH adsorption. HCOOH was obtained from an external HCOOH droplet. The HCOOH droplet was added on the sample of Ru/Al_2O_3 and Al_2O_3 in air. Afterward, the sample was pumped to low vacuum of 5×10^{-3} mbar over 24 h at RT. **Exp. VII** HCOOH hydrogenation. To determine the hydrogenation properties of HCOOH on Ru/Al_2O_3 and Al_2O_3, the samples were exposed to 1 bar of H_2 after Exp VI and then heated to 300 °C with a rate of 1 °C/min.

In addition, solid reference samples of Na_2CO_3, $CaCO_3$, $NaHCO_3$, and $KHCO_3$ were analyzed by transmission FT-IR to obtain the infrared bands of CO_3^{2-} and HCO_3^{-}.

Gaussian Fittings. Four regions were separately fitted: 2100−1800 cm^{-1}, 1800−1530 cm^{-1}, 1530−1420 cm^{-1}, and 1420−1350 cm^{-1}. The baseline of each region was taken as a linear function. The position, width, and height of each Gaussian contribution were all constrained. The initial values of these constraints were taken from a combination of an estimation of the peak ranges observed in the spectra and the measured peaks of the reference samples. These initial parameters were used to simulate all the peaks in these ranges from all the experiments. The results of a fitting run were used to give the new values of parameters and constraint ranges for the next fitting run. This process was iterated manually hundreds of times until two criteria were met: (1) all the peaks followed regular and physically meaningful trends as the reaction proceeded, and (2) subsequently fits did not change the parameters of the peak position, height, and width.

The combination of the measurement of the reference samples and the Gaussian fittings through the reaction coordination helped to identify and assign the observed peaks.

3. RESULTS AND DISCUSSION

3.1. Correlations of Coexisting Adsorption Species in the CO_2 Hydrogenation Reaction. In order to learn what species come out during CO_2 hydrogenation, we triggered CO_2 hydrogenation reaction on Ru/Al_2O_3 by mixing CO_2 and H_2 followed by program heating (Exp. I). Figure 1(a) shows

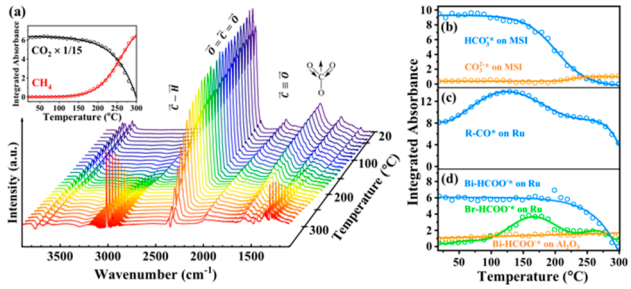

Figure 1. (a) Infrared absorbance spectra with the insertion of CO_2 to CH_4 conversion during CO_2 hydrogenation (Exp. I) and evolution of adsorption species of (b) $HCO_3^{-}*$ with a peak at 1650 cm^{-1} and $CO_3^{2-}*$ with a peak at 1450 cm^{-1} located at MSI, (c) R-CO* on Ru, and (d) Bi-$HCOO^{-}*$ on Ru, Br- and Br-$HCOO^{-}*$ on Ru, and Bi-$HCOO^{-}*$ on Al_2O_3. In (b)−(d), circles are the original data of integrated peak intensity from Gaussian fittings, and the lines are the nonlinear fittings of those original data.

the main reaction of CO_2 converting to CH_4 from 100 °C. The variations in the complex peaks below 2200 cm^{-1} suggest the development of adsorption species from CO_2 and H_2 coadsorption during the hydrogenation reaction. The peaks were distinguished in three regions: C−O stretching of adsorbed carbon monoxide (CO*) between 2100 and 1800 cm^{-1}; O−C−O stretching of adsorbed bicarbonates ($HCO_3^{-}*$), carbonates ($CO_3^{2-}*$), and formate ($HCOO^{-}*$) between 1700 and 1400 cm^{-1}; and C−H and O−H bending between 1400 and 1200 cm^{-1} (Figure 1(a)). To identify the infrared peaks, we measured reference samples of carbonates, bicarbonates, and surface formic acid on Ru/Al_2O_3 and Al_2O_3 (Figures S1 and S2). More importantly, we resolved the peaks of the adsorbates of each reaction using Gaussian fittings

DOI: 10.1021/acs.jpcc.8b06508
J. Phys. Chem. C 2018, 122, 20888−20893

Table 1. Vibrational Modes and Infrared Peak Positions (cm^{-1}) of the Reference Samples and the Reaction Species from This Work[a]

species	C−H as. str.	C−H b.	C═O str.	O−C−O as. str.	O−C−O s. str.	O−C−O b.	O−H b.	C−OH str.
CO_3^{2-}	--	--	1776	1454	1454	880	--	--
CO_3^{2-}*[b,c23]	--	--	--	1500	1450	--	--	--
HCO_3^-	--	--	1695	1650, 1630	1402, 1371	--	1305	1007
HCO_3^-*[b,c20,23−27]	--	--	1690	1650	1440	--	1230	--
HCOOH[c28−30]	2940, 2871	1415	1748, 1670	1620, 1560 (on Al_2O_3)	1405, 1360	--	1220	970
Bi-HCOO−*[b,d] on Ru	2913, 2895, 2870	1390	1720	1620	1405	--	1220	970
Br-HCOO−*[b,d] on Ru	2913, 2895, 2870	1390	1720	1590	1375	--	1220	970
Bi-HCOO−*[b,d] on Al_2O_3[c31]	2918, 2895, 2870	1387	1710	1560	1360	--	1230	970

species	C≡O as. str.
linear-CO*[b] on $Ru^{\delta+}$[c26,30,32−35]	2060
linear-CO*[b] on Ru^0[c26,30,32−35]	2035
linear-CO*[b] on $Ru^0/Ru^{\delta+}$[c26,30,32−35]	2015
bridged-CO*[b] on Ru[c26,30,32−35]	1990, 1950, 1905
gaseous CO	2150

[a]str.: stretching. as.: asymmetric. s.: symmetric. b.: bending. (w): weak. [b]* indicates adsorbed state. [c]The corresponding bond vibrations and infrared peak positions are comparable to the given references. [d]The way to distinguish bidentate and bridged structures of formate is as follows: bidentate-HCOO−* has the splitting value of O−C−O asymmetric (ν_{as}) and symmetric (ν_s) stretching, $\Delta\nu = \nu_{as} - \nu_s$, less than 220 cm^{-1}, and bridged-HCOO−* has $\Delta\nu$ in the range of 220−280 cm^{-1}.[36]

(Figure S3). The peak assignments are summarized in Table 1 based on the combination of reference peaks and Gaussian fittings.

At RT, four types of adsorption species were formed during the CO_2 hydrogenation reaction on Ru/Al_2O_3: HCO_3^-*, CO_3^{2-}*, CO*, and $HCOO^-$*. HCO_3^-* were formed by reaction of CO_2 with the surface hydroxyl groups on the Al_2O_3 support following the H_2 pretreatment. The intensity of HCO_3^-* was larger on Ru/Al_2O_3 than on bare Al_2O_3, and HCO_3^-* on Al_2O_3 could not be continuously formed from CO_2 on Al_2O_3 (Figures S4 and S5), indicating the adsorption of HCO_3^-* is increased by the metal−support interface (MSI). As shown in Figure 1(b), during the temperature ramp the concentration of HCO_3^-* was initially constant and started to decrease above about 150 °C. CO_3^{2-}* increased gradually with increasing temperature above 200 °C, and the increase most likely came from HCO_3^-* deprotonation. Assuming that the peak intensities for O−C−O stretching are similar in HCO_3^-* and CO_3^{2-}* at the same site and coverage, the much lower intensity of CO_3^{2-}* indicates that only some of the HCO_3^-* decomposed to CO_3^{2-}*, and the remaining HCO_3^-* molecules were consumed in other processes, for instance, desorption or decomposition.

Reactive CO* (R-CO*) with the peaks at 2015, 1990, 1950, and 1905 cm^{-1} (Table 1 and Figure S6) increased from RT up to 150 °C (Figure 1(c)) and then decreased, indicating that its production was slower than its consumption above 150 °C. At 220 °C, R-CO* concentration leveled off, possibly because a new route of R-CO* production became active. Nevertheless, linear-CO* on Ru^0 at 2035 cm^{-1} (Table 1) remained constant throughout the entire experiment, indicating the inert character of this species (Figure S6). It has been reported that hydrogen-perturbed CO could locate in the range between 1840 and 1700 cm^{-1} and could be H_2CO species or carbonyl hydrides and formyl/formaldehyde.[21,22] In our case, we did not have peaks between that region as shown in Figure S6. The discrepancy between the reference and our work could be originated by the different effects of different catalyst surfaces which are sensitive/selective to the different adsorption species.

$HCOO^-$* is present in three forms: bidentate on Ru with a high frequency of 1620 cm^{-1}, bridged on Ru with a frequency of 1590 cm^{-1}, and bidentate on Al_2O_3 with a frequency of 1560 cm^{-1} (Table 1). Bidentate-$HCOO^-$* (Bi-$HCOO^-$*) on Ru was abundant and stable up to 220 °C, after which it was consumed and completely disappeared at 300 °C. Conversely, bridged-$HCOO^-$* (Br-$HCOO^-$*) on Ru increased from 70 to 160 °C, followed by a slow decrease (Figure 1(d)). Bidentate-$HCOO^-$* (Bi-$HCOO^-$*) on Al_2O_3 showed only one weak peak at 1560 cm^{-1} (Figure 1(d)). The slight increase in production of this species, instead of consumption, indicates it is not reactive during CO_2 hydrogenation.

3.2. Unraveling the Roles of Individual Species Using in Situ Control. The temperature-dependent evolution of the above-mentioned species shows correlations with the CO_2 methanation reaction. However, their simultaneous existence makes the determination of their origins and roles in the reaction equivocal. To unravel these mysteries, we isolate the adsorption species step by step in the following sections.

3.2.1. Interactions of CO_2 and the Surface. We first investigated the interactions between CO_2 and the surface by replacing H_2 with He, keeping all other conditions the same (Exp. II). The results are shown in Figure 2(a)−(c). At RT, HCO_3^-* was the main species formed when the surface was exposed in CO_2, indicating that it is the primary product of CO_2 adsorption (Figure 2(a)). HCO_3^-* decreased almost linearly with increasing temperature after 50 °C. Simultaneously, CO_3^{2-}* increased almost linearly with increasing temperature. These trends are similar to those in the CO_2 hydrogenation reaction (Figure 1(b)). The higher ratio of CO_3^{2-}*/HCO_3^-* for CO_2 adsorption than that for CO_2 hydrogenation reflects the more favorable deprotonation of HCO_3^-* in H_2-deficient conditions.

All the CO* showed the same peaks as those in CO_2 hydrogenation except for a 25 cm^{-1} redshift of the peak of linear-CO* at 2035 cm^{-1} (Figure S7). This redshift was probably due to the adsorption of linear-CO* onto the oxidized metal surface ($Ru^{\delta+}$) in a hydrogen-deficient environment. This linear-CO* at 2035 cm^{-1} showed no change in the whole process, as same insensitiveness as in the CO_2

DOI: 10.1021/acs.jpcc.8b06508
J. Phys. Chem. C 2018, 122, 20888−20893

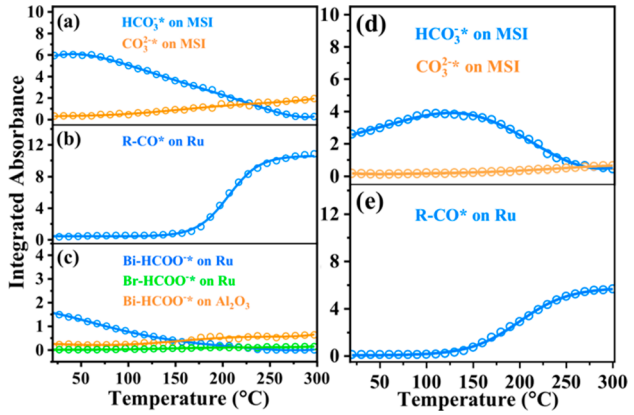

Figure 2. (a) HCO_3^-* and CO_3^{2-}*, (b) R-CO*, (c) three structural $HCOO^-$* during CO_2 adsorption reaction (Exp. II), (d) HCO_3^-* and CO_3^{2-}*, and (e) R-CO* during HCO_3^-* decomposition (Exp. III). The peak positions were the same as in Figure 1. The circles are the original data of integrated peak intensity from Gaussian fittings, and the lines are the nonlinear fittings of those original data.

hydrogenation reaction (Figure S7). Notably, R-CO* increased above 150 °C (Figure 2(b)). This increase in R-CO* production explains the plateau in R-CO* concentration starting at 220 °C in CO_2 hydrogenation (Figure 1(c)). However, whether these CO* were produced from the decomposition of CO_2 or HCO_3^-* is not clear yet and needed further controlling experiments.

Bi-$HCOO^-$* on Ru at RT had much weaker intensity (Figure 2(c)) than the corresponding intensity when H_2 was present (Figure 1(d)). The intensity decreased with increasing temperature until complete disappearance at 220 °C. We speculate that Bi-$HCOO^-$* is not formed from HCO_3^-* since $HCOO^-$* does not increase when HCO_3^-* decreases. Rather, Bi-$HCOO^-$* must be formed by CO_2 reacting with adsorbed H atoms on the surface. Thus, we conclude that there must be a small amount of residual H atoms present in this experiment and that the small concentration of H explains the small concentration of Bi-$HCOO^-$*. Br-$HCOO^-$* on Ru was almost invisible, indicating that CO_2, HCO_3^-*, and CO* do not form Br-$HCOO^-$* in a hydrogen-deficient environment. Bi-$HCOO^-$* on Al_2O_3 slightly increased above 150 °C when Bi-$HCOO^-$* on Ru disappeared possibly due to migration of Bi-$HCOO^-$* on Ru to Al_2O_3 support.[15]

3.2.2. In Situ Isolation and Decomposition of HCO_3^-.* To determine whether CO* was formed from the decomposition of CO_2 or HCO_3^-*, we pumped out the gases after CO_2 adsorption at RT (Exp. III). In this way, we produced a surface exclusively covered by HCO_3^-* at RT. The catalyst was then heated. Broadly speaking, during heating HCO_3^-* decreased (Figure 2(d)) starting from 130 °C, and there was a corresponding increase in R-CO* concentration (Figure 2(e)), excluding the inert linear-CO* at 2065 cm^{-1} (Figure S8). Thus, we conclude that the R-CO* originates from HCO_3^-* and not from CO_2. The 20 °C lower temperature than the onset temperature of R-CO* formation in CO_2 adsorption reaction (Figure 2(b)) is probably the reason for released active sites in a high vacuum. We currently do not have an explanation for the increase in HCO_3^-* at the beginning of the temperature ramp, but the broad conclusion stands.

3.2.3. In Situ Isolation and Hydrogenation of CO.* To find out which adsorption species can react to form CH_4, we hydrogenated them separately by preparing them individually with in situ control.

We first isolated all the CO* in situ from HCO_3^-* decomposition following the process shown in Figure 2(d) and (e) and cooling to RT. One bar of H_2 was then filled followed by program heating (Exp. IV). As shown in Figure 3(a) and (b), R-CO* decreased, and CH_4 increased starting at

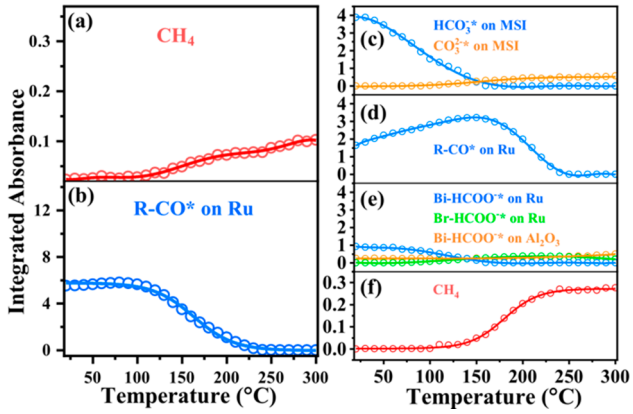

Figure 3. (a) Production of CH_4 and (b) reduction of CO* during R-CO* hydrogenation (Exp. IV). Evolution of (c) HCO_3^-* and CO_3^{2-}*, (d) R-CO*, (e) three structural $HCOO^-$*, and (f) CH_4 during HCO_3^-* hydrogenation (Exp. V). The peak positions were the same as in Figure 1. The circles are the original data of integrated peak intensity from Gaussian fittings, and the lines are the nonlinear fittings of those original data.

120 °C. Note that this onset temperature is 20 °C higher than that observed in the CO_2 hydrogenation reaction (Figure 1(a)) probably because of the lower R-CO* concentration in this case. Linear-CO* at 2040 cm^{-1} was still inert in this hydrogenation process (Figure S9). Thus, we conclude R-CO* is clearly an intermediate in the CH_4 formation reaction, while the linear-CO* above 2035 cm^{-1} is a byproduct.

3.2.4. In Situ Isolation and Hydrogenation of HCO_3^-.* Next, we investigate whether HCO_3^-* is an intermediate. HCO_3^-* was obtained in situ from CO_2 adsorption followed by pumping to high vacuum at RT (Exp. V). As shown in Figure 3(c)−(e), when the sample was heated in H_2, HCO_3^-* concentration decreased immediately until completely consumed at 150 °C. Meanwhile, R-CO* and Bi-$HCOO^-$* on Ru were immediately produced at RT. There is a corresponding increase in the concentration of R-CO* which is the result of surface RWGS reaction triggered by HCO_3^-* hydrogenation at MSI. Thus, we conclude that HCO_3^-* is an intermediate in the overall reaction, producing CO* which is subsequently converted to CH_4 (Figure 3(f)).

3.2.5. Role of $HCOO^-$.* Finally, we consider whether $HCOO^-$* is an intermediate. Unfortunately, we were unable to produce isolated $HCOO^-$* by in situ control because HCO_3^-* was always present when $HCOO^-$* was produced. Nonetheless, we have evidenced that Bi-$HCOO^-$* on Ru formed in our in situ control is a reaction intermediate. Figure 1(d) shows that in the CO_2 hydrogenation reaction Bi-$HCOO^-$* on Ru formed from CO_2 hydrogenation and was consumed in the same shape of the reactive species of CO_2, HCO_3^-*, and R-CO* above 220 °C. This consumption could involve the formation reaction of CO* or CH_4. In Figure 3(e), when there was no CO_2, Bi-$HCOO^-$* on Ru was formed by the previous step of CO_2 adsorption reacting with residual hydrogen on the

DOI: 10.1021/acs.jpcc.8b06508
J. Phys. Chem. C 2018, 122, 20888−20893

surface. Bi-$HCOO^{-}$* on Ru started to decrease at a 40 °C lower temperature than the onset temperature of CH_4 formation. Therefore, we conclude that Bi-$HCOO^{-}$* on Ru is reduced by hydrogen to form CO* instead of directly to CH_4. Additionally, Bi-$HCOO^{-}$* on Ru could convert to the bridged form on Ru from 70 to 160 °C as illustrated in Figure 1(d) and Figure 3(e). This Br-$HCOO^{-}$* on Ru could be reduced above 160 °C but not completely when it was abundant (Figure 1(d)). However, it kept constant above 160 °C when it had low concentration. This implies that Br-$HCOO^{-}$* on Ru has a high activation energy of hydrogenation. Bi-$HCOO^{-}$* on Al_2O_3 was a byproduct as it always slowly increased by the migration of $HCOO^{-}$* on Ru in all the experiments.

The distinct reactivities between the $HCOO^{-}$* of different adsorption structures on Ru can be understood by the atomic structure of the surface. The distance between neighboring Ru atoms in a hexagonal structure is 2.71 Å, while the distance between the two oxygen atoms of formate is 2.20 Å. These two comparable distances facilitate adsorption of the bridged structure of formate to the surface of the bulk Ru, where the two oxygen atoms bind to two adjacent Ru atoms. A larger distance between Ru atoms, e.g., at the edge or defect where some Ru atoms are isolated, is required to accept Bi-$HCOO^{-}$* on Ru so that two oxygen atoms bind to one Ru atom. Therefore, the bulk sites of the surface result in the stable Br-$HCOO^{-}$* on Ru, and the edge or defect centers promote the high reactivity of Bi-$HCOO^{-}$* on Ru.

We also prepared isolated $HCOO^{-}$* by ex situ application of a drop of HCOOH to the sample in air followed by pumping to vacuum. All the forms of $HCOO^{-}$* on Ru/Al_2O_3 were reactive and started to form CO* above 150 °C (Figure S2). Above 220 °C, Bi-$HCOO^{-}$* on Ru and on Al_2O_3 were substantially reduced, leading to CO* formation slowing down and CH_4 formation. Br-$HCOO^{-}$* on Ru was not reduced completely. The ex situ experiment supports the conclusion that Bi-$HCOO^{-}$* on Ru is a reaction intermediate, and Br-$HCOO^{-}$* on Ru possesses high activation energy of reduction; however, on the other hand, it showed a discrepancy with the in situ experiment where Bi-$HCOO^{-}$* on Al_2O_3 was also reactive. The discrepancy is not surprising given that the ex situ experiment involved exposure to air and the high acidity of the sample. The discrepancy points out the danger of obtaining misleading results by ex situ preparation.

4. CONCLUSIONS

The results we have just described can be understood in terms of the reaction mechanisms summarized in Figure 4. There are two pathways to CO_2 methanation. One is initiated by HCO_3^{-}* formation, illustrated by the green arrow. The other is initiated by the formation of Bi-$HCOO^{-}$* on Ru, illustrated by the orange arrow. In the HCO_3^{-}* pathway, first, HCO_3^{-}* is formed at RT when CO_2 adsorbs and reacts with the surface hydroxyl groups on the metal−support interface which originated from the H_2 prereduction of the surface. Next, the HCO_3^{-}* is reduced to CO* by hydrogen at RT. HCO_3^{-}* also produces CO* via thermal decomposition above 130 °C in high vacuum and above 170 °C in a CO_2- and H_2-rich environment. The temperature shift is due to competition for adsorption sites. In the Bi-$HCOO^{-}$* pathway, the first step is the reaction of CO_2 and hydrogen to produce Bi-$HCOO^{-}$* on Ru at RT. This species then reacts with hydrogen to produce CO* on Ru at RT. Alternatively, Bi-$HCOO^{-}$* on Ru converts

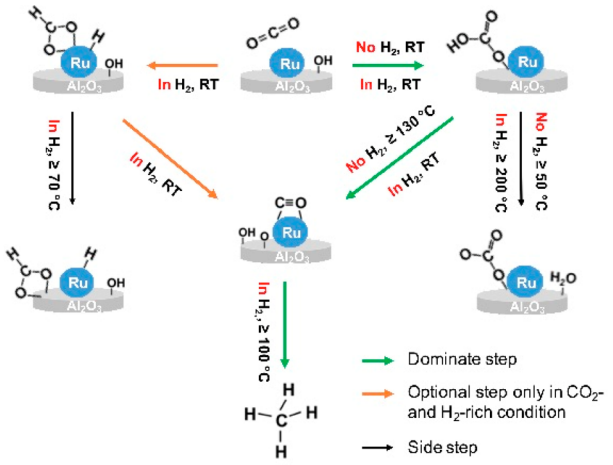

Figure 4. Schema of the hydrogenation steps of CO_2 on Ru/Al_2O_3.

to more stable Br-$HCOO^{-}$* on Ru which has a higher activation energy to reaction and does not fully convert under our conditions (not shown in the figure). In both pathways, the final process is the hydrogenation of R-CO* to CH_4 above 100 °C. R-CO* is consequently a key intermediate in CO_2 methanation.

In addition to the pathways leading to CH_4 formation, there are also notable side reactions that lead to nonreactive byproducts. As shown by the black arrow on the right side of Figure 4, HCO_3^{-}* decomposes to CO_3^{2-}* at 50 °C in a hydrogen-deficient environment and at 200 °C in a hydrogen-rich environment. The black arrow on the left side of Figure 4 shows that Bi-$HCOO^{-}$* on Ru converts to Bi-$HCOO^{-}$* on Al_2O_3. Besides, linear-CO* on Ru^0 forms along with R-CO* but also is insensitive to the hydrogenation reaction (not shown in the figure).

In summary, we unraveled the surface reaction mechanism of CO_2 hydrogenation via in situ control of the individual formation and hydrogenation of each adsorption species in operando DRIFTS combined with iterative Gaussian fitting. $CO_2 \rightarrow HCO_3^{-}* \rightarrow CO* \rightarrow CH_4$ is the dominate reaction step which takes place from the metal−support interface to the metal surface. This gives us the effective pathway and surface sites for CO_2 methanation.

■ ASSOCIATED CONTENT

Supporting Information

The Supporting Information is available free of charge on the ACS Publications website at DOI: 10.1021/acs.jpcc.8b06508.

Infrared spectra of all the experiments, the evolution of each vibrational mode of each species, and the explanation of bicarbonate adsorption at MSI are illustrated (PDF)

■ AUTHOR INFORMATION

Corresponding Authors

*E-mail: andreas.zuettel@epfl.ch.
*E-mail: kun.zhao@epfl.ch.

ORCID

Kun Zhao: 0000-0002-7182-8089

Notes

The authors declare no competing financial interest.

DOI: 10.1021/acs.jpcc.8b06508
J. Phys. Chem. C 2018, 122, 20888−20893

■ ACKNOWLEDGMENTS

SCCER HeE which is financially supported by the Innosuisse - Swiss Innovation Agency is greatly acknowledged. K.Z. also thanks Daniel Auerbach for the full discussions and revisions of this work.

■ REFERENCES

(1) Züttel, A.; Mauron, P.; Kato, S.; Callini, E.; Holzer, M.; Huang, J. Storage of Renewable Energy by Reduction of CO_2 with Hydrogen. *Chimia* **2015**, *69*, 264−268.
(2) Kato, S.; Matam, S. K.; Kerger, P.; Bernard, L.; Battaglia, C.; Vogel, D.; Rohwerder, M.; Züttel, A. The Origin of the Catalytic Activity of a Metal Hydride in CO_2 Reduction. *Angew. Chem., Int. Ed.* **2016**, *55*, 6028−6032.
(3) Weatherbee, G. D.; Bartholomew, C. H. Hydrogenation of CO2 on Group VIII metals IV. Specific Activities and Selectivities of Silica-Supported Co, Fe, and Ru. *J. Catal.* **1984**, *87*, 352−362.
(4) Jalama, K. Storage of Renewable Energy by Reduction of CO_2 with HydrogenCarbon Dioxide Hydrogenation over Nickel-, Ruthenium-, and Copper-based Catalysts: Review of Kinetics and Mechanism. *Catal. Rev.: Sci. Eng.* **2017**, *59*, 95−164.
(5) Frontera, P.; Macario, A.; Ferraro, M.; Antonucci, P. L. Supported Catalysts for CO_2 Methanation: A Review. *Catalysts* **2017**, *7*, 59.
(6) Homs, N.; Toyir, J.; Piscina, P. R. Catalytic Processes for Activation of CO_2. *New and Future Developments in Catalysis: Activation of Carbon Dioxide, Chapter 1*; Suib, S. L., Ed.; Elsevier, 2013; pp 1−26.
(7) Ge, Q. F. Mechanistic Understanding of Catalytic CO_2 Activation from First Principles Theory. *New and Future Developments in Catalysis: Activation of Carbon Dioxide, Chapter 3*; Suib, S. L., Ed.; Elsevier, 2013; pp 49−79.
(8) Wang, W.; Wang, S. P.; Ma, X. B.; Gong, J. L. Recent Advances in Catalytic Hydrogenation of Carbon Dioxide. *Chem. Soc. Rev.* **2011**, *40*, 3703−3727.
(9) Maitlis, P. M.; Quyoum, R.; Long, H. C.; Turner, M. L. Towards a Chemical Understanding of the Fischer−Tropsch Reaction: Alkene Formation. *Appl. Catal., A* **1999**, *186*, 363−374.
(10) van Santen, R. A.; Markvoort, A. J.; Filot, I. A. W.; Ghouri, M. M.; Hensen, E. J. M. Mechanism and Microkinetics of the Fischer−Tropsch Reaction. *Phys. Chem. Chem. Phys.* **2013**, *15*, 17038−17063.
(11) Filot, I. A. W.; van Santen, R. A.; Hensen, E. The Optimally Performing Fischer−Tropsch Catalyst. *Angew. Chem.* **2014**, *126*, 12960−12964.
(12) Munnik, P.; Jongh, P. E.; Jong, K. P. Recent Developments in the Synthesis of Supported Catalysts. *Chem. Rev.* **2015**, *115*, 6687−6718.
(13) Vlasenko, V. M.; Yuzefovich, G. E. Mechanism of the Catalytic Hydrogenation of Oxides of Carbon to Methane. *Russ. Chem. Rev.* **1969**, *38*, 728−739.
(14) Garbarino, G.; Bellotti, D.; Finocchio, E.; Magistri, L.; Busca, G. Methanation of Carbon Dioxide on Ru/Al_2O_3: Catalytic Activity and Infrared Study. *Catal. Today* **2016**, *277*, 21−28.
(15) Marwood, M.; Doepper, R.; Renken, A. In-situ Surface and Gas Phase Analysis for Kinetic Studies under Transient Conditions The catalytic hydrogenation of CO_2. *Appl. Catal., A* **1997**, *151*, 223−246.
(16) Marwood, M.; Vyve, F. V.; Doepper, R.; Renken, A. Periodic Operation Applied to the Kinetic Study of CO_2 Methanation. *Catal. Today* **1994**, *20*, 437−448.
(17) Prairie, M. R.; Renken, A.; Highfield, J. G.; Thaimpi, K. R.; Grätzel, M. A Fourier Transform Infrared Spectroscopic Study of CO_2 Methanation on Supported Ruthenium. *J. Catal.* **1991**, *129*, 130−144.
(18) Eckle, S.; Anfang, H. G.; Behm, J. Reaction Intermediates and Side Products in the Methanation of CO and CO_2 over Supported Ru Catalysts in H_2-Rich Reformate Gases. *J. Phys. Chem. C* **2011**, *115*, 1361−1367.
(19) Miao, B.; Ma, S. S. K.; Wang, X.; Su, H. B.; Chan, S. H. Catalysis Mechanisms of CO_2 and CO Methanation. *Catal. Sci. Technol.* **2016**, *6*, 4048−4058.
(20) Wang, F.; He, S.; Chen, H.; Wang, B.; Zheng, L. R.; Wei, M.; Evans, D. G.; Duan, X. Active Site Dependent Reaction Mechanism over Ru/CeO_2 Catalyst toward CO_2 Methanation. *J. Am. Chem. Soc.* **2016**, *138*, 6298−6305.
(21) Sápi, A.; Halasi, G.; Kiss, J.; Dobó, D. G.; Juhász, K. L.; Kolcsár, V. J.; Ferencz, Z.; Vári, G.; Matolin, V.; Erdőhelyi, A.; Kukovecz, Á; Kónya, Z. In Situ DRIFTS and NAP-XPS Exploration of the Complexity of CO_2 Hydrogenation over Size-Controlled Pt Nanoparticles Supported on Mesoporous NiO. *J. Phys. Chem. C* **2018**, *122*, 5553−5565.
(22) Fisher, I. A.; Bell, A. T. A Comparative Study of CO and CO_2 Hydrogenation over Rh/SiO_2. *J. Catal.* **1996**, *162*, 54−65.
(23) Taifan, W.; Boily, J. F.; Baltrusaitis, J. Surface Chemistry of Carbon Dioxide Revisited. *Surf. Sci. Rep.* **2016**, *71*, 595−671.
(24) Rudolph, W. W.; Fischer, D.; Irmer, G. Vibrational Spectroscopic Studies and Density Functional Theory Calculations of Speciation in the CO_2-Water System. *Appl. Spectrosc.* **2006**, *60*, 130−144.
(25) Rudolph, W. W.; Irmer, G.; Königsberger, E. Speciation Studies in Aqueous HCO_3^-−CO_3^{2-} Solutions. A combined Raman spectroscopic and thermodynamic study. *Dalton Trans.* **2008**, 900−908.
(26) Garbarino, G.; Bellotti, D.; Finocchio, E.; Magistri, L.; Busca, G. Methanation of Carbon Dioxide on Ru/Al_2O_3: Catalytic Activity and Infrared Study. *Catal. Today* **2016**, *277*, 21−28.
(27) Miao, B.; Ma, S. S. K.; Wang, X.; Su, H. B.; Chan, S. H. Catalysis Mechanisms of CO_2 and CO Methanation. *Catal. Sci. Technol.* **2016**, *6*, 4048−4058.
(28) Chang, Y. T.; Yamaguchi, Y.; Miller, W. H.; Schaefer, H. F., III An Analysis of the Infrared and Raman Spectra of the Formic Acid Dimer $(HCOOH)_2$. *J. Am. Chem. Soc.* **1987**, *109*, 7245−7253.
(29) Zelsmann, H. R.; Marechal, Y. The Raman and IR Spectra of HCOOH and DCOOD Crystals at Low Temperature. *J. Mol. Struct.* **1976**, *29*, 357−368.
(30) Chin, S. Y.; Williams, C. T.; Amiridis, M. D. J. FTIR Studies of CO Adsorption on Al_2O_3- and SiO_2-Supported Ru Catalysts. *J. Phys. Chem. B* **2006**, *110*, 871−882.
(31) Busca, G.; Lamotte, J.; Lavalley, J. C.; Lorenzelli, V. FT-IR Study of the Adsorption and Transformation of Formaldehyde on Oxide Surfaces. *J. Am. Chem. Soc.* **1987**, *109*, 5197−5202.
(32) Szanyi, J.; Kwak, J. H. Dissecting the steps of CO_2 reduction: 2. The Interaction of CO and CO_2 with Pd/γ-Al_2O_3: an In Situ FTIR Study. *Phys. Chem. Chem. Phys.* **2014**, *16*, 15126−15138.
(33) Vogt, C.; Groeneveld, E.; Kamsma, G.; Nachtegaal, M.; Lu, L.; Kiely, C. J.; Berben, P. H.; Meirer, F.; Weckhuysen, B. M. Unravelling Structure Sensitivity in CO_2 Hydrogenation over Nickel. *Nat. Catal* **2018**, *1*, 127−134.
(34) Hadjiivanov, K. I.; Vayssilov, G. N. Characterization of Oxide Surfaces and Zeolites by Carbon Monoxide as an IR Probe Molecule. *Adv. Catal.* **2002**, *47*, 307−511.
(35) Hoffmann, F. M. Infrared Reflection-Absorption Spectroscopy of Adsorbed Molecules. *Surf. Sci. Rep.* **1983**, *3*, 107−192.
(36) Shido, T.; Asakura, K.; Iwasawa, Y. Reactant-Promoted Reaction Mechanism for Catalytic Water-Gas Shift Reaction on MgO. *J. Catal.* **1990**, *122*, 55−67.

DOI: 10.1021/acs.jpcc.8b06508
J. Phys. Chem. C 2018, 122, 20888−20893